Materials Characterization 155 (2019) 109811

Contents lists available at ScienceDirect

Materials Characterization

journal homepage: www.elsevier.com/locate/matchar

Effect of heat treatment on the microstructure and shape memory behaviour of Fe-Mn-Si-Ni-Cr alloys

Isidro Esquivel[a,b], María Florencia Giordana[b], Ana Velia Druker[a,b,*]

[a] Facultad de Cs. Ex., Ingeniería y Agrimensura (UNR), Av Pellegrini 250, Rosario, Argentina
[b] Instituto de Física Rosario (CONICET-UNR), Bv. 27 de Febrero 210 bis, Rosario, Argentina

ARTICLE INFO

Keywords:
Fe-Mn-Si shape memory alloys
Microstructure
Martensitic transformation
TEM

ABSTRACT

The effect of chemical composition and thermomechanical treatments on both the mechanical properties and the shape memory (SM) capacity of Fe-based SM alloys was investigated by X-ray diffraction and optical and transmission-electron microscopy analysis. We produced the Fe-17Mn-6Si-10Cr-5Ni and Fe-22Mn-3Si-10Cr-5Ni alloys (17Mn and 22Mn, respectively) and measured the degree of shape recovery (DSR) after tension and bending for samples rolled and annealed in different conditions. We found that the 17Mn alloy rolled at 1000 °C and annealed at 700 °C had the highest DSR, i.e. 78%. After tension, the microstructure contained nanometre sized stress-induced ε-martensite plates in a matrix composed of dislocations, SFs and precipitates. On the other hand, after tensile deformation, the dislocation density observed in the 22Mn sample rolled at 1000 °C and annealed at 700 °C was higher than before tension. This alloy's low 48% DSR is a consequence of permanent, nonrecoverable plastic deformation.

1. Introduction

The shape memory effect (SME) observed in non-thermoelastic Fe-Mn-Si based alloys is due to the reversible stress-induced γ (FCC) ↔ ε (HCP) martensitic transformation. The reverse transformation is activated by heating above a critical temperature [1,2] and some pseudo elasticity (PE) is occasionally observed upon unloading [3]. Because of the relative low production cost and good mechanical properties of these alloys, they are considered in many mechanical and civil engineering applications.

Since Sato et al. [4] discovered 9% recovery strain in Fe-30Mn-1Si[1] single crystals, extensive research has been conducted to optimize the polycrystalline shape memory alloys (SMAs) and to find industrial applications. It is generally agreed that the main parameters affecting the SME are the alloy's stacking fault energy (SFE) and the microstructure and texture of the austenitic phase.

According to the review of Sade et al. [5], the Fe-Mn-Si based SMAs usually contain between 15 and 30% Mn, in order to stabilize the FCC → HCP transformation. A lower Mn content decreases the ε-martensite stability, while increasing that of the α´-martensite (BCC). In fact, if the amount of Mn is lowered, the increase in Ms. temperature needs to be compensated by the addition of 4–5% Ni. Usually, up to 6% Si is added to control the SFE and the austenite antiferromagnetic ordering temperature (Néel temperature). To improve the corrosion resistance 5–9% Cr is generally added. But, when the Cr quantities are above 7%, the brittle Fe-Cr sigma phase ($\sigma_{Fe\text{-}Cr}$) can form [6]. In such cases, Ni is added to prevent σ phase formation, in a manner similar to that for stainless steels [7]. In 1990, Otsuka et al. [6] introduced the polycrystalline Fe-28Mn-6Si-5Cr, Fe-20Mn-5Si-8Cr-5Ni and Fe-16Mn-5Si-12Cr-5Ni alloys, which combine good corrosion resistance and a good SME. Nevertheless, these alloys only exhibited 2.5% or less recovery strain.

Recently, Lai et al. [8] summarized the effort devoted to improving the SME of these alloys and their derivatives, which has occurred over the past 35 years. Although training produces an increase in the yield strength of the austenite and a decrease in the critical stress for martensitic transformation, it is a necessary but not sufficient process for improving the SME. A high density of uniformly distributed stacking faults (SFs) [9–11] on the primary slip planes of the austenite is characteristically developed during training. This microstructure is considered indispensable for the formation of the specific martensite plates that occur upon mechanical loading and which produce a shape change [9–11]. In 2001, Kajiwara et al. [12,13] reported an increase in the recovery strain after the precipitation of fine NbC particles, thus avoiding the expensive training treatments. Contrarily, Stanford and Dunne [14,15] and Baruj et al. [16] suggested that under certain

* Corresponding author at: Facultad de Cs. Ex., Ingeniería y Agrimensura (UNR), Av Pellegrini 250, Rosario, Argentina.
E-mail address: druker@ifir-conicet.gov.ar (A.V. Druker).

[1] Chemical compositions will always be expressed as wt%.

https://doi.org/10.1016/j.matchar.2019.109811
Received 4 March 2019; Received in revised form 3 July 2019; Accepted 4 July 2019
Available online 05 July 2019
1044-5803/ © 2019 Elsevier Inc. All rights reserved.

circumstances these precipitates do not necessarily lead to an improvement of the SME. They even observed a detrimental effect for rather small NbC precipitates (< 5 nm).

Finally, it was demonstrated that the SM behaviour may be controlled by simply applying thermomechanical treatments to a material with the appropriate chemical composition [15–18]. Only the Mn content seems to be a controversial point. Let's look at some articles published in the last year:

V. Paleu et al. [19] discussed the application of Fe-28Mn-6Si-9Cr SMA for self-adjustable, axial-preload control in angular contact bearings. Lai et al. [8] studied the role of VC precipitation in a Fe-28Mn-6Si-5Cr-0.764 V-0.18C SMAs. Balagurov et al. [20] investigated the changes of the direct and reverse martensitic transition during thermocycling over the phase transition in Fe-22Mn-3Si, Fe-26Mn-4Si and Fe-26Mn-7Si alloys. Ju et al. [21] studied an Fe-15Mn-5Si-12Cr-6Ni SMA laser welded with a powder filling. Kim et al. [22] severely plastically deformed an Fe-13.51Mn-4.82Si-8.32Cr-3.49Ni-0.15C SMA and found the factors that affect the recovery stress and recovery strain. Peng et al. [23] studied an as cast polycrystalline Fe-19Mn-5.5Si-9Cr-4.5Ni alloy and proposed that the coarsening of austenitic grains is key for achieving high recovery strains. Our group has been investigating the Fe-15Mn-5Si-9Cr-5Ni (nominal composition) SMA for many years and obtained interesting results. Nevertheless, different quantities of undesirable ferrite appear under certain processing conditions [24–27]. The presence of ferrite not only affects the mechanical properties but also degrades the SM capacity because the quantity of transformative austenite is reduced.

Undoubtedly, tailoring the microstructure – in order to introduce a high density of evenly distributed stacking faults throughout a properly strengthened austenite matrix – is key in promoting shape memory behaviour in these Fe-based alloys [24]. Many investigations have studied the effect of grain size, typically extreme sizes. For example, Kim et al. [22] analysed small grains - about 1 μm -, Wang et al. [28] studied grains up to 250 μm, and Wen et al. [29] observed “giant” grains. In our research, we concentrate on the standard variability of grain sizes obtained by industrial processes, in which good mechanical and shape memory properties must be combined. Keeping this in mind, and taking into account the variety of SMAs that are discussed in the literature, we produced two alloys, called 17Mn and 22Mn. We subjected these materials to various thermomechanical treatments, and performed X-ray diffraction, and optical and transmission-electron microscopy analysis. In view of some specific technological applications, i.e. shaft and pipe couplings, [26] we determined the degree of shape recovery (DSR) after tension and bending and found the conditions – chemical composition and thermomechanical treatment – that provide the highest DSR. The aim was to discern which aspects of the microstructure account for the SM properties.

2. Materials and methods

The Fe-17Mn-6Si-10Cr-5Ni and Fe-22Mn-3Si-10Cr-5Ni alloys (nominal composition; from now on we will refer to them as 17Mn and 22Mn, respectively) were prepared in an induction furnace operating at 10 KHz and 30 KW. Commercial raw material was melted in high purity alumina crucibles and cast into rectangular moulds, providing a shape suitable for rolling. The ingots were homogenised at 1150 °C for 3 h. The chemical composition of each alloy is given in Table 1. Sections of the cast blocks were rolled into sheets with a 1 mm final thickness and then annealed at different temperatures, as described in Table 2.

Hardness was measured in six different points of each sample using a Digimess AHT-RC-(T) hardness tester with an applied load of 600 N (Rockwell “A” scale).

Shape memory properties were determined after tensile and bending tests at room temperature. Under this pre-deformation condition, the production and handling processes would be as simple as possible and more attractive for industrial applications.

Table 1
Chemical composition of the alloys after the homogenization treatment.

Alloy	Method	Fe	C	Mn	Si	Cr	Ni	SFE[a] (mJ/m^2)
17Mn	(**)	62.88	0.09	16.59	6.49	9.06	4.89	1.53
17Mn	EDS-SEM	61.09	NM	17.16	6.31	9.67	5.26	2.36
22Mn	AES	59.90	0.03	21.30	3.27	10.40	4.54	14.79
22Mn	(**)	62.10	0.07	21.04	4.10	8.44	4.32	12.84

(**) C: IRAM850/71; Si: IRAM858/71; Cr: ASTM E353/93; Mn, Ni: Atomic Absorption Spectroscopy.
EDS-SEM: Energy-dispersive X-ray Spectroscopy performed with Scanning Electron Microscopy.
AES: Atomic Emission Spectroscopy.
NM: Not measured.
[a] Calculated according to Li et al. [30].

Table 2
Thermomechanical treatments applied to the alloys and their nomenclature. Annealing treatments lasted 30 min.

Alloy	Rolling temperature, °C	Annealing temperature, °C	Nomenclature
17Mn	650	700	**A**
		800	**B**
	1000	700	**C**
		800	**D**
		1000	**E**
22Mn	650	700	**F**
		800	**G**
	1000	700	**H**
		800	**I**
		1000	**J**

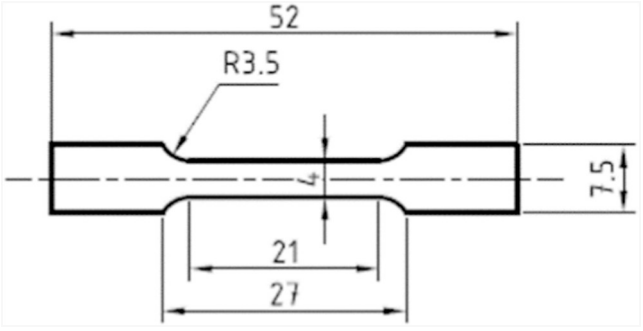

Fig. 1. Dimensions and form of the tensile specimens (mm).

We cut dog-bone specimens for tensile tests from the rolled sheets by electric discharge machining (Fig. 1).

The tensile deformation was performed in an Instron 3382 universal testing machine. The strain was measured using a 10 mm gauge length extensometer and the specimens were deformed at 0.06 mm/min up to 4% engineering strain, at room temperature. Fig. 2 shows the stress-strain curves of samples **C** and **H**, which are representative of the batches. Elastic and pseudoelastic relaxation and remaining strain are indicated in the figure as ε_e, ε_{pe} and ε_r, respectively. Samples were deformed elastically to a yield stress of σ_y. From this point, deformation can be due to the $\gamma \rightarrow \varepsilon$ martensitic transformation and/or dislocation glide. Table 3 lists the σ_y values measured of each sample. Since the cross section of each tensile specimen can vary locally due to irregularities of the thickness and/or width, we assume a relative experimental error of ± 5% in the stresses measured.

In order to calculate accurately the degree of tensile shape recovery (DSR_t), we used three pairs of Vickers indentations distributed along the gauge length and on both sides of each sample, parallel to the specimen axis. Every pair of indentations represents an l_0 reference distance of 10 mm. The indentations were made before any deformation of the sample, by a Shimadzu micro-hardness tester equipped with a

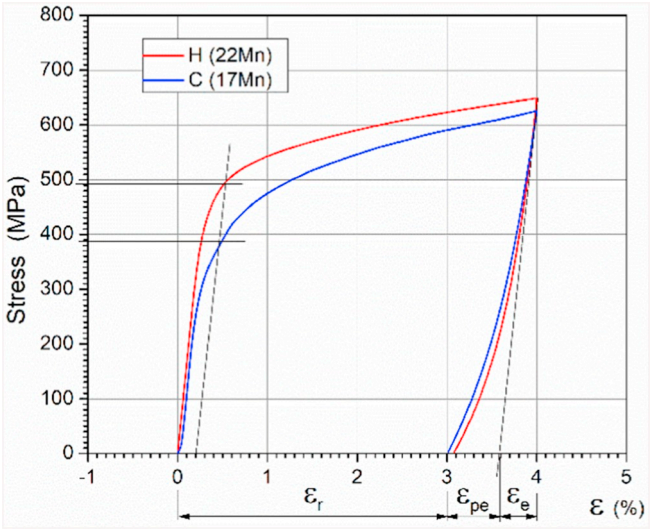

Fig. 2. Tensile-deformation, stress-strain curves obtained from samples **C** and **H**.

Table 3
Mechanical and SM properties of samples A to J.

Alloy	Sample	Processing: rolling temp. (°C); annealing temp. (°C).	Yield stress (MPa)	Hardness (HRA)	DSR_b (%)	DSR_t (%)
17 Mn	**A**	650; 700	765 ± 40	69 ± 1	80 ± 2	56 ± 4
	B	650; 800	640 ± 30	67 ± 2	59 ± 2	40 ± 3
	C	1000; 700	390 ± 20	60 ± 2	88 ± 2	78 ± 4
	D	1000; 800	360 ± 20	57 ± 2	87 ± 2	78 ± 4
	E	1000; 1000	–	56 ± 1	47 ± 2	–
22 Mn	**F**	650; 700	640 ± 30	64 ± 2	58 ± 2	57 ± 4
	G	650; 800	510 ± 25	61 ± 2	22 ± 2	39 ± 3
	H	1000; 700	490 ± 25	61 ± 2	60 ± 2	48 ± 3
	I	1000; 800	420 ± 20	56 ± 2	31 ± 2	31 ± 3
	J	1000; 1000	–	54 ± 2	26 ± 2	–

micrometer screw with a precision of 0,01 mm. The degree of tensile shape recovery (DSR_t) was determined as follows:

$$DSR_t(\%) = \frac{l_1 - l_2}{l_1 - l_0} \cdot 100$$

where l_0 and l_1 are the distances between each pair of Vickers indentations before and after deformation, respectively, and l_2 is the distance after the recovery anneal at 550 °C for 5 min (this is above the Af temperature).

To perform the bending tests, we cut specimens 90 mm long and $1 \times 3\,mm^2$ in cross section from the rolled sheets. These bars were bent 90° around a 40 mm diameter mandrel at room temperature, as shown in Fig. 3. Thus, the pre-strain (ε_b) is:

$$\varepsilon_b(\%) = \frac{t}{D + t} \cdot 100 = 2.5\%$$

We photographed the samples before and after annealing, and we measured the remaining angle after relaxation and the recovered angles, θ_1 and θ_2 respectively. We assume an error of ± 1°. The degree of shape recovery, DSR_b, was calculated as:

$$DSR_b(\%) = \frac{\theta_2}{\theta_1} \cdot 100$$

Samples for microstructural analysis were mechanically and electrolytically polished in an 80–20 (vol%) acetic-perchloric acid solution at room temperature and 27 V. Microstructural analyses were performed using a PME3 Olympus optical microscope (OM) and a JEOL JEM-2100 plus scanning-transmission electron microscope (STEM) operating at 200 kV with a LaB_6 electron gun. TEM specimens were electropolished using the double-jet technique in a 90–10 (vol%) acetic-perchloric acid solution at room temperature. X-ray diffraction patterns were measured using the Cu-Kα_1/Kα_2 lines in a Philips X-pert pro MPD goniometer operating at 40 kV and 30 mA. The scans were carried out from 30 to 85°, in 0.02° 2θ steps, with a collection time of 10 s per step.

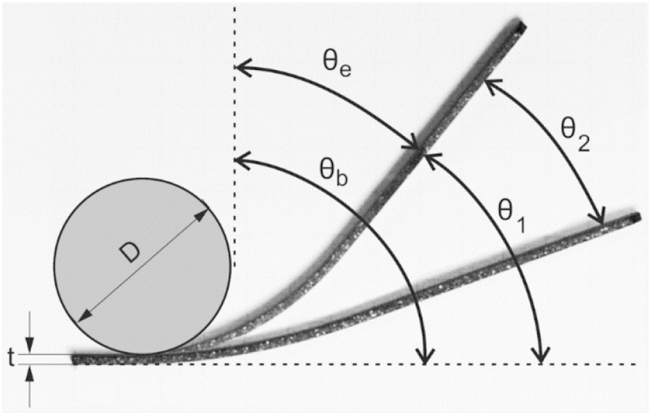

Fig. 3. Schematic drawing of the bending test. θ_b: applied bending angle. θ_e: elastic plus pseudoelastic relaxation angle. θ_1: remaining angle after relaxation. θ_2: recovered angle.

3. Results

3.1. Mechanical and shape memory tests

We subjected the alloys to various processing conditions and determined the mechanical and shape memory properties. It is well known that testing conditions, i.e. magnitude of pre-strain and testing temperature, have an important influence on the SM properties and then, on the DSR. Consequently, we analysed the SM properties using just certain pre-strain values, i.e. 4% and 2.5% in tensile and bending tests, respectively. These values evidenced to be effective for usual mechanical applications because higher deformations deteriorate the DSR and lower values produce insufficient dimensional shift.

Table 3 lists the results corresponding to samples **A** through **J**, and Fig. 4 shows the relationship between the degree of shape recovery in bending and the annealing temperature for both alloys and rolling temperatures.

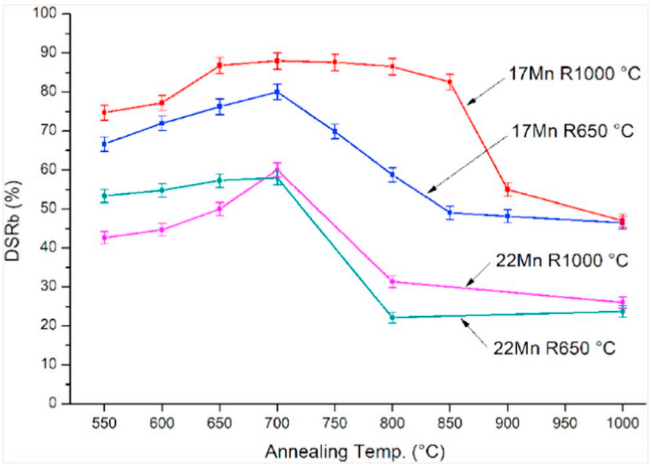

Fig. 4. Relationship between the degree of shape recovery in bending and the annealing temperature for both alloys and rolling temperatures.

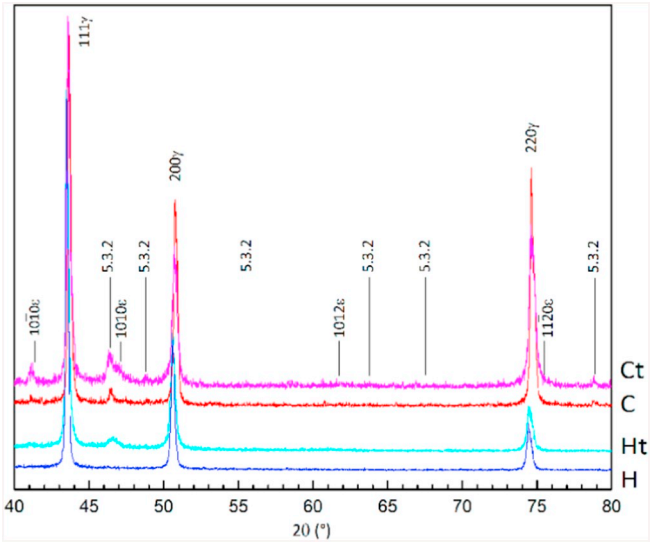

Fig. 5. X-ray diffraction patterns from samples **C** and **H** before and after 4% tensile deformation – **Ct** and **Ht**.

These results show that the SM properties of the 17Mn alloy are better than for the 22Mn material. Particularly, the 17Mn alloy rolled at 1000 °C is more stable with respect to the annealing temperature. The highest DSR values, for both alloys, were obtained from samples rolled at 1000 °C and annealed at 700 °C, samples **C** and **H**.

3.2. X-ray diffraction analysis

X-ray diffraction measurements determined the phases present in samples from each processing condition. Particularly, we looked for the presence of the brittle sigma phase ($\sigma_{Fe\text{-}Cr}$), ferrite, and thermal martensite (ε_t). However, none of these components was found.

Fig. 5 shows the diffraction patterns from samples **C** and **H** before and after tensile deformation to induce the martensitic transformation. Before deformation, the main peaks corresponded to the austenitic matrix (FCC) and a number of shorter peaks indicated the presence of the 5.3.2 precipitate [27]. These features were common for all the samples. After deformation – samples **Ct** and **Ht** – small peaks corresponding to stress-induced ε-martensite (HCP) were identified in the diffraction patterns. Table 4 lists the phases encountered for each sample.

3.3. Microstructural analysis

In order to understand the origins of the shape memory behaviour, we examined the internal structure of the samples in the austenitic state, i.e. before deformation to induce the martensitic transformation. OM and TEM characterization techniques were used to determine the effects of chemical composition, rolling temperature and annealing temperature on changes in the defect distribution. We also prepared TEM specimens from samples after the martensitic transformation occurred, analysing the martensite formation with tensile tests.

Table 4
Phases encountered for each sample.

Sample	Phases			Sample	Phases		
A	γ FCC	p.p.t 5.3.2	–	**F**	γ FCC	–	–
B	γ FCC	p.p.t 5.3.2	–	**G**	γ FCC	p.p.t 5.3.2	–
C	γ FCC	p.p.t 5.3.2	–	**H**	γ FCC	p.p.t 5.3.2	–
Ct	γ FCC	p.p.t 5.3.2	ε HCP	**Ht**	γ FCC	p.p.t 5.3.2	ε HCP
D	γ FCC	p.p.t 5.3.2	–	**I**	γ FCC	p.p.t 5.3.2	–
E	γ FCC	p.p.t 5.3.2	–	**J**	γ FCC	–	–

3.3.1. Optical microscopy characterization

The microstructure observed at the OM scale, tends to be nonuniform in both geometry and grain size, as shown in Fig. 6. Grain boundary delineation is not complete in some images, probably due to the variation of misorientation. We also found that twins extended beyond individual grains, which would correspond to boundaries with low misorientation angles [31].

3.3.1.1. Effect of the rolling temperature:. Images corresponding to samples **A**, **B**, **F** and **G** show that rolling at low temperature elongates grains along the rolling direction (see Fig. 6a). Soft lines, like grain subboundaries, would indicate that dislocations organized into low-energy configurations (polygonization). On the other hand, dynamic recrystallization activated during rolling at 1000 °C. This is indicated by more regular shaped grains (Fig. 6c and d).

3.3.1.2. Effect of the annealing temperature:. After annealing above 800 °C, the grain size and shape tend to be more uniform (Fig. 6b and c). Twins appear in the 22Mn alloy (Fig. 6c), but they are not seen in samples **B** and **D**, corresponding to the 17Mn alloy (Fig. 6a and b). Particularly, annealing at 1000 °C intensified the features associated with recrystallization. At this high annealing temperature all the grains are twinned in both alloys, as can be seen in images of samples **E** and **J** (Fig. 6d).

3.3.1.3. Effect of chemical composition:. The main difference between OM images is the number of precipitates. They were present in the as-homogenised condition and then elongated with rolling. Fig. 6b shows that the smaller precipitates form bands and the bigger ones align.

The X-ray diffraction results (Fig. 5/Table 4) show a higher precipitate density in the 17Mn alloy samples than for the 22Mn alloy. Particle size is very diverse: from 0.5 to 1 μm for those precipitates located at grain boundaries, to bigger and more massive particles in the bulk material (note the one identified by the white arrow in Fig. 6a). Some black lines or spots can be seen alternating with clear zones in the massive precipitates. These marks are equivalent to what was reported by Vandeer Voort and James [32] and Druker et al. [26].

The quantity of precipitates also varies with heat treatments. Annealing at 800 °C strongly increases precipitation, while the treatments at 1000 °C significantly reduce the volume fraction of particles (Fig. 6c). Fuster et al. [27] found that this phase dissolves into the austenitic matrix for treatments above 1000 °C.

3.3.2. TEM characterization

3.3.2.1. 17Mn alloy. The microstructure of the 17Mn alloy rolled at 650 °C and annealed at 700 °C (sample **A**) is shown in Fig. 7. A high density of dislocations (D) and stacking faults (SF) appear in the austenite grains that comprise the bright field (BF) TEM image in Fig. 8a. The selected area electron diffraction pattern (SADP) inserted in the image shows some double spots (circled). This pattern indicates the presence of nanotwins (NT), which can be seen in the magnified view in Fig. 7b. We also observed a few precipitates, which do not appear in the images.

When the same alloy rolled at 650 °C is annealed at 800 °C (sample **B**), the matrix contains only a few dislocations, stacking faults in several directions and lots of precipitates. These microstructural features indicate that the strongly deformed material recrystallized during the heat treatment. Fig. 8a shows SFs in contact with a grain boundary and other SFs lying in the matrix. In addition, the volume of precipitates grew at this temperature, which can be seen in the OM image, Fig. 6a. The precipitates vary in size between 80 and 1000 nm. Fig. 8b shows the interaction between the precipitates (P) and perfect dislocations.

The microstructure of the 17Mn alloy after rolling at 1000 °C and annealing at 700 °C (sample **C**) is composed of dislocation arrays, stacking faults and small precipitates, as shown in Fig. 9a. Two variants of SFs were identified from the SADP inset in Fig. 9b. The SFs are

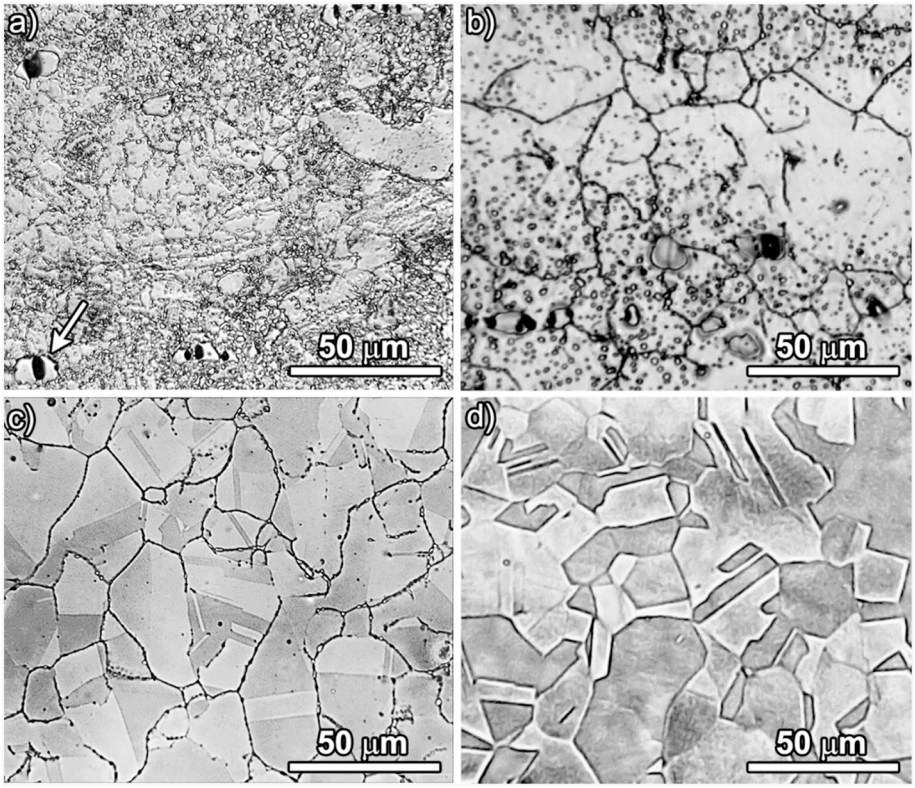

Fig. 6. OM images corresponding to samples: a) **B**, 17Mn rolled at 650 °C and annealed at 800 °C, b) **D**, 17Mn rolled at 1000 °C and annealed at 800 °C, c) **I**, 22Mn rolled at 1000 °C and annealed at 800 °C, d) **J**, 22Mn rolled at 1000 °C and annealed at 1000 °C.

aligned parallel to the traces of the $(\bar{1}11)\gamma$ and the $(1\bar{1}1)\gamma$ planes.

Annealing at 800 °C recrystallized the alloy rolled at 1000 °C (sample **D**). The TEM image in Fig. 9a shows some bands and fine SFs. The SFs tend to form rectangular networks in the $[\bar{2}\bar{1}1]\gamma$ and $[1\bar{2}1]\gamma$ directions, as indexed from the SADP in Fig. 10b. Also, many particles precipitated during this annealing, as can be seen in the OM image, Fig. 6b. We recorded a SADP from a precipitate located at the grain boundary, which measured 170 × 500 nm. The pattern, shown in Fig. 10c, corresponds to a cubic $Fe_5Ni_3Si_2$ type intermetallic of the space group $P2_13$, as identified by Fuster et al. [27]. The characteristic reflections of this phase are identified as 5.3.2 in the diffractograms shown in Fig. 5 and in Table 4.

After annealing at 1000 °C (sample **E**), the austenite grains appear free of dislocations. Three variants of SFs and few precipitates are observed in Fig. 11a. Faults of a single variant appear on both sides of a twin in a 38 µm grain, as shown in Fig. 11b.

3.3.2.2. 22Mn alloy. A microstructure consisting of austenite grains containing stacking faults and a high density of dislocations, which form cell like arrays is shown in Fig. 12 for the 22Mn alloy rolled at 650 °C and annealed at 700 °C (sample **F**). The SFs were indexed to have two variants from the SADP inset in Fig. 12a.

After annealing at 800 °C (sample **G**), long extended SFs seem to be emitted from grain-boundary ledges, which appear in the lower left corner of Fig. 13, in the manner documented by Meyers and Murr [32] and Inagaki [33]. Overlapping stacking faults originate from closely-spaced {111} planes. The image also shows the distortions created by the interaction between SFs and between the SFs and the precipitates.

The microstructure of the 22Mn alloy rolled at 1000 °C and annealed at 700 °C (sample **H**) is shown in Fig. 14. Small quantities of stacking faults, dislocations, precipitates and some twins are seen in the austenite matrix. The elastic distortion contrast that appears around precipitates shows that there is (some) coherence with the matrix [27].

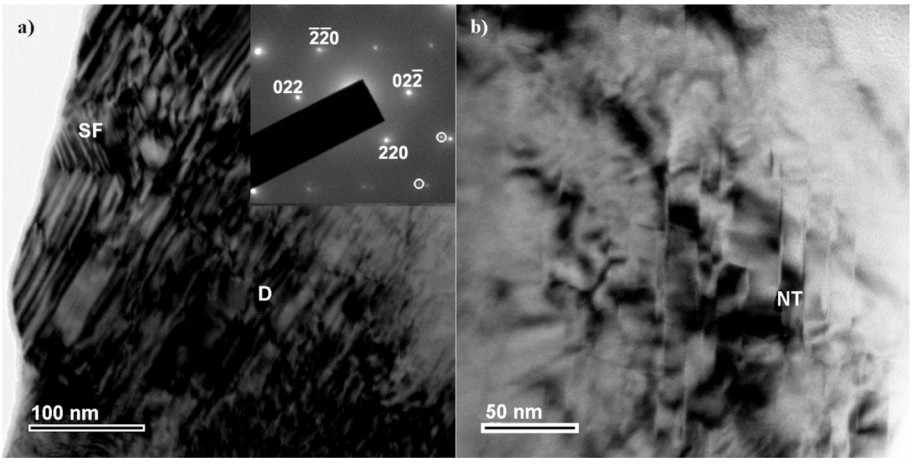

Fig. 7. Microstructure of the 17Mn alloy rolled at 650 °C and annealed at 700 °C, sample **A**. a) TEM image showing a high density of dislocations (D) and stacking faults (SF) in the austenite matrix. The inset selected area electron diffraction pattern (SADP) was recorded at the $[111]\gamma$ zone axis. b) Nanotwins (NT) are seen at a higher magnification.

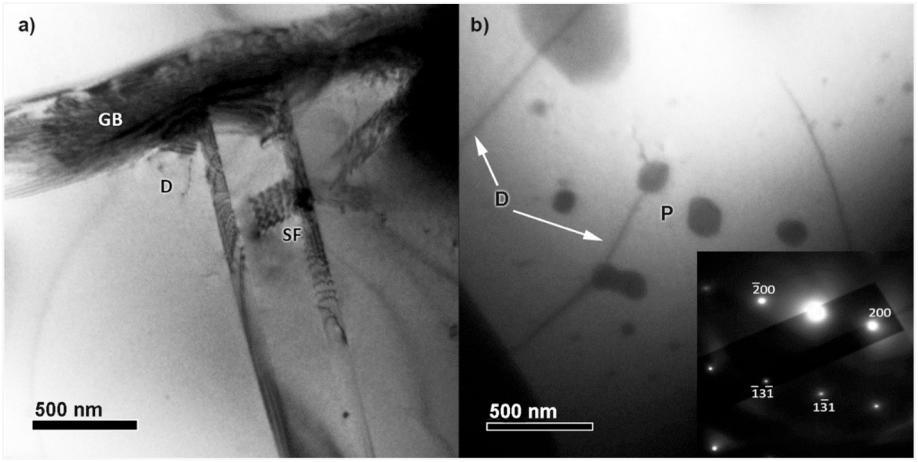

Fig. 8. Same alloy as in Fig. 7 but annealed at 800 °C, sample **B**. The matrix contains only a few dislocations (D), stacking faults (SF) in several directions and precipitates. a) SFs in contact with a grain boundary (GB) are also limited by other SFs. b) precipitates (P) interacting with perfect dislocations. Zone axis: $[013]_\gamma$.

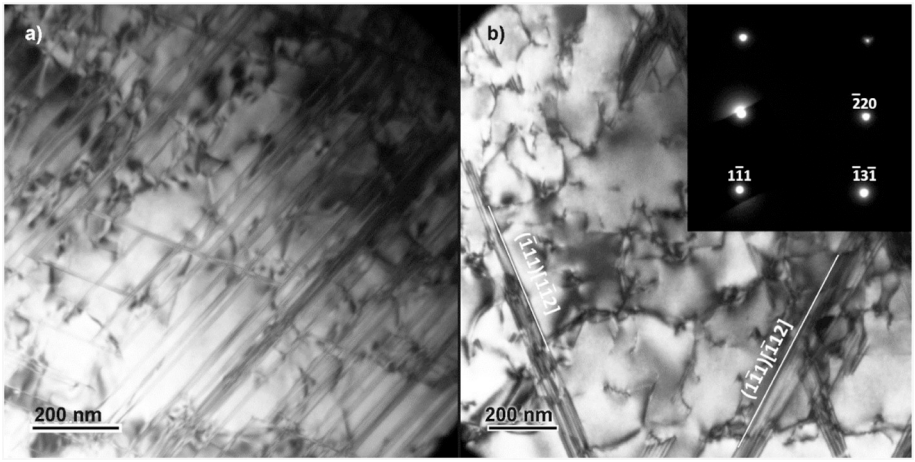

Fig. 9. Microstructure of the 17Mn alloy rolled at 1000 °C and annealed at 700 °C, sample **C**. a) The austenite matrix contains dislocation arrays, stacking faults and small precipitates. b) Two variants of SFs are indicated in the figure. The inset corresponds to the selected area electron diffraction pattern (SAEDP); the zone axis is $[111]_\gamma$.

The lower magnification image in Fig. 14b shows a high density of dislocations close to a grain boundary (GB) and the precipitates located there. The size of these particles is around 150 nm.

After annealing at 800 °C (sample **I**), the structure of the alloy rolled at 1000 °C contains stacking faults, twins and dissociated dislocations (DD). The images in Fig. 15a and b, show a stepped grain boundary and

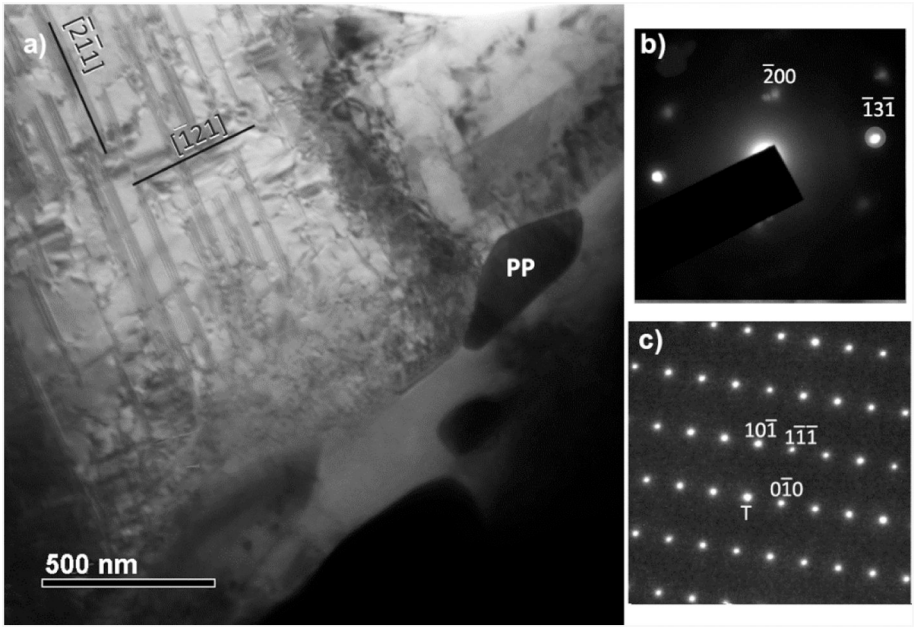

Fig. 10. Same alloy as in Fig. 9 but annealed at 800 °C, sample **D**. a) The TEM image shows a few dislocations and SFs in two directions indexed with the SAEDP shown in b). The zone axis is $[113]_\gamma$. c) SAEDP recorded at the $[101]_{P23}$ zone axis taken from one of the precipitates located at the grain boundary. The precipitate's dimensions are 170 × 500 nm.

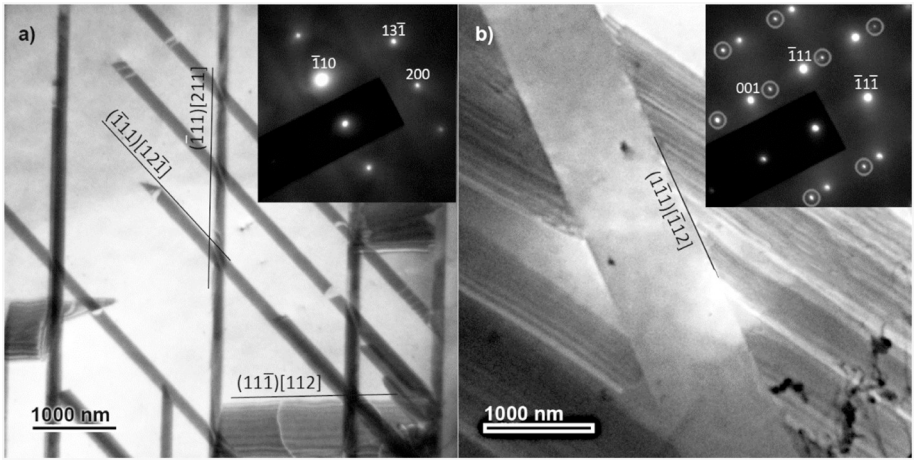

Fig. 11. Same alloy as in Fig. 9 but annealed at 1000 °C, sample **E**. The microstructure has very few dislocations, lots of SFs and a few small precipitates. a) The three SF variants were indexed from the SADP inset in the figure. The zone axis is [11$\bar{2}$]γ. b) TEM image showing stacking faults limited by twin boundaries. The circled dots in the diffraction pattern are due to the twins. The zone axis is [011]γ.

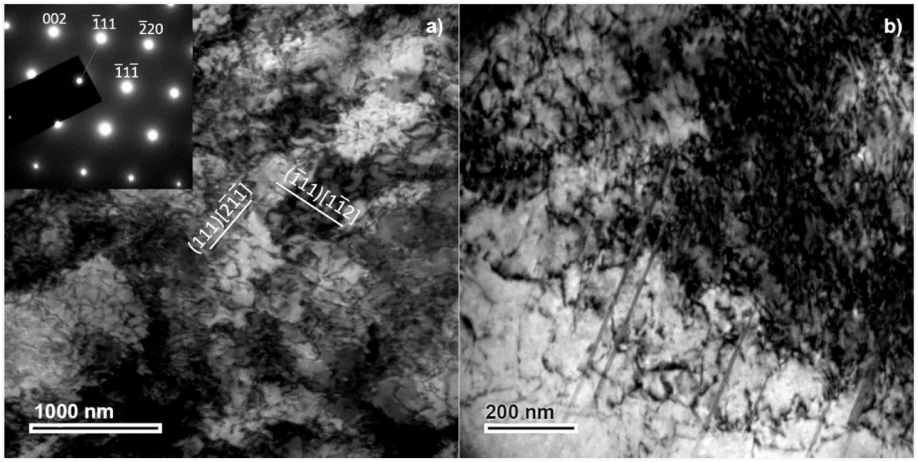

Fig. 12. Microstructure of the 22Mn alloy rolled at 650 °C and annealed at 700 °C, sample **F**. a) The austenite matrix contains a high density of dislocations forming arrays and stacking faults. The inset corresponds to the SAEDP; the zone axis is [110]γ. b) A higher magnification image from the same region.

a parallel-sided twin interrupting the development of the SFs.

The structure after annealing at 1000 °C (sample **J**) is rather similar to that of sample **I** except for the grain size (see Fig. 6d). No dislocations are seen in the matrix. The low magnification TEM images in Fig. 16 illustrate the interaction between defects. Fig. 16a shows stacking faults nucleating at a grain boundary and dissociated dislocations. A few small precipitates are indicated by the black arrows. Fig. 16b shows an incomplete parallel-sided twin inhibiting the development of the SFs.

We also analysed the structure of the samples that showed the best SM performance, after tensile deformation to induce the martensitic transformation.

Fig. 17 shows the microstructure of the 17Mn alloy rolled at 1000 °C and annealed at 700 °C after 4% room-temperature tensile deformation (sample **Ct**). The traces of two {111} planes indicated by white letters in Fig. 17a, a bright field image, are parallel to [011]. We see a large number of thin plates on the ($\bar{1}$11) plane, but only few plates on the ($\bar{1}\bar{1}$1) plane. These plates are ε-martensite, as indicated by the hcp spots in the inset of Fig. 17b, a dark field image. The dark field image was taken from the circled yellow spot (i.e. 01$\bar{1}$1). The zone axes of the diffraction pattern are [011]γ //[11$\bar{2}$0]ε.

Fig. 18, a bright field image of the 22Mn alloy rolled at 1000 °C and annealed at 700 °C, (sample **Ht**) shows a few thin ε-martensite plates and a high density of dislocations and SFs. This alloy was given the same 4% tensile deformation as sample **Ct**.

4. Discussion

The decision to increase the Mn content (to improve the SM properties) was effective because no ferrite is present in the microstructure of the 17Mn and the 22Mn alloys. The parent phase is mainly austenitic and the quantity of 5.3.2 precipitates is greater in the 17Mn alloy, as shown in Table 4 and Fig. 6. After the different thermo-mechanical treatments, the samples were subjected to shape memory tests and the degrees of shape recovery (DSR) are listed in Table 3. The OM and TEM images shown in Figs. 6 and 7 to 16 show the microstructures that are described above. As was expected, the differences in these results are a consequence of the internal modifications due to the processing applied to the alloys.

Firstly, one clearly sees that the SM behaviour of the 17Mn alloy is much better than that of the 22Mn composition. After rolling at 650 °C and annealing at 700 °C, the DSR of sample **A** is almost 22% greater than that for sample **F**, i.e. 80 and 58%, respectively. The microstructural features indicate that the matrix preserves the defects introduced during the rolling. Clearly, deformation at this temperature acts as "cold working" and no sign of recrystallization is observed in the material after the annealing at 700 °C. Nevertheless, austenite grains of the 17Mn alloy are hardened enough (yield stress: 750 MPa against 640 MPa in sample **F**) to avoid perfect dislocation gliding, and the density of SFs also appears higher than in the 22Mn alloy. In addition,

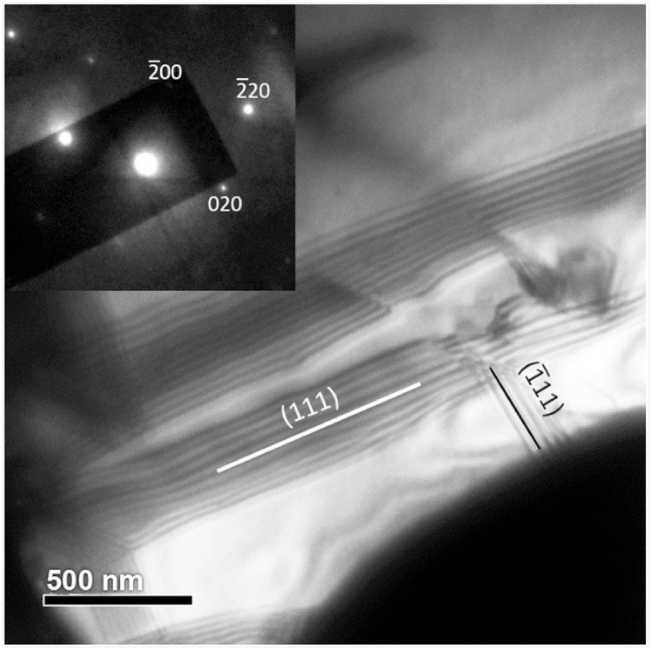

Fig. 13. Same alloy as in Fig. 12 but annealed at 800 °C, sample **G**. Overlapping stacking faults were emitted on closely-spaced (111) planes and on a $(\bar{1}11)$ plane. The image also shows the interaction between SFs and the precipitates. The zone axis is near $[001]_\gamma$.

nanoscale twins (NTs) formed in sample **A** during the rolling deformation. They act as obstacles to perfect dislocation glide because they progressively subdivide the austenite grains and lower the dislocation mean free path. This process is known as the dynamic Hall-Petch effect. Due to the exceptionally small size of the nano-twins (about 10 nm), as well as their high density, dislocation movement is effectively hindered [34]. However, looking at the values of shape recovery, apparently the NTs do not affect the direct and reverse movement of partial dislocations along the same path. A high number of NTs is formed in the 17Mn alloy during this thermo-mechanical process, confirming that the SFE is very low (see Table 1). Also, the high dislocation density can be the reason for the formation of partial dislocation sources, which are then responsible for the formation of SFs and twins. On the other hand, twins about 1000–1100 nm in thickness are regarded as one of the important factors that decrease the SME because deformation by twinning cannot be recovered through heating [10,31,32]. The 22Mn samples processed in all conditions show those kinds of thick twins, which impede the glide of other partial dislocations on noncoplanar slip systems (Figs. 11b and 16b). In fact, samples **E**, **G**, **I** and **J**, which have largely twinned structures, show the poorest shape memory behaviour. Twins and ε-martensite are planar defects associated with the overlapping of stacking faults. Ledges in grain boundaries act as dislocation sources in low stacking-fault energy materials where the dislocations have split into partials connected by a stacking fault [32]. It would be interesting to analyse both phenomena relative to the grain boundaries in ferrous shape memory alloys. GBs can stop the advance of SFs by impeding their development and/or be a

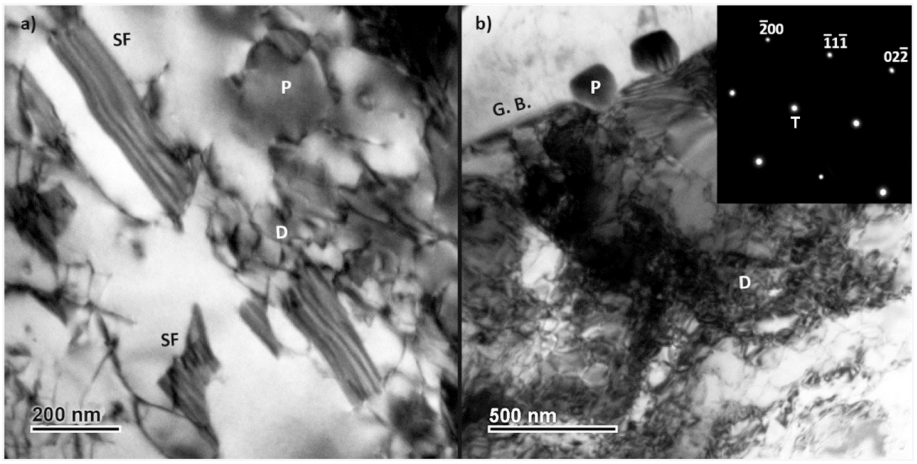

Fig. 14. Microstructure of the 22Mn alloy rolled at 1000 °C and annealed at 700 °C, sample **H**. a) Stacking faults, dislocations, precipitates and some twins appear in the austenite matrix. b) The lower magnification image shows a high density of dislocations close to a grain boundary and precipitates located in the GB. The zone axis is $[011]_\gamma$.

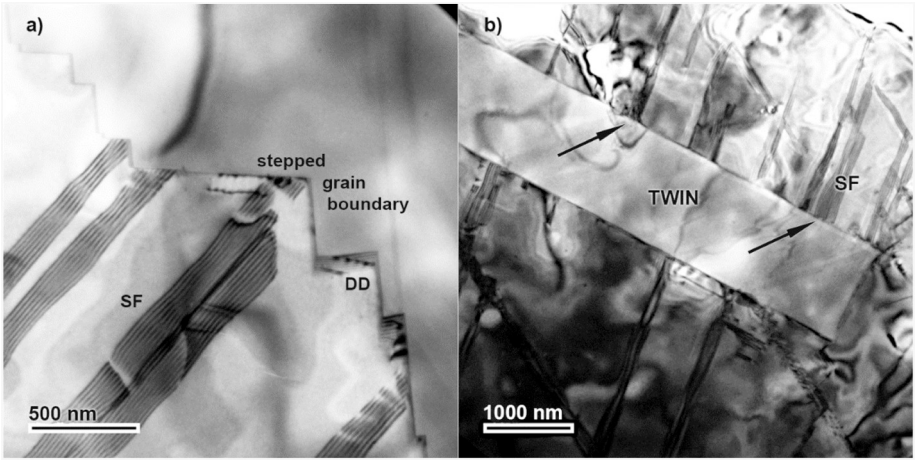

Fig. 15. Same alloy as in Fig. 14 but annealed at 800 °C, sample **I**. Stacking faults, twins and some dissociated dislocations (DD) are located at: a) a stepped grain boundary, and b) a twin.

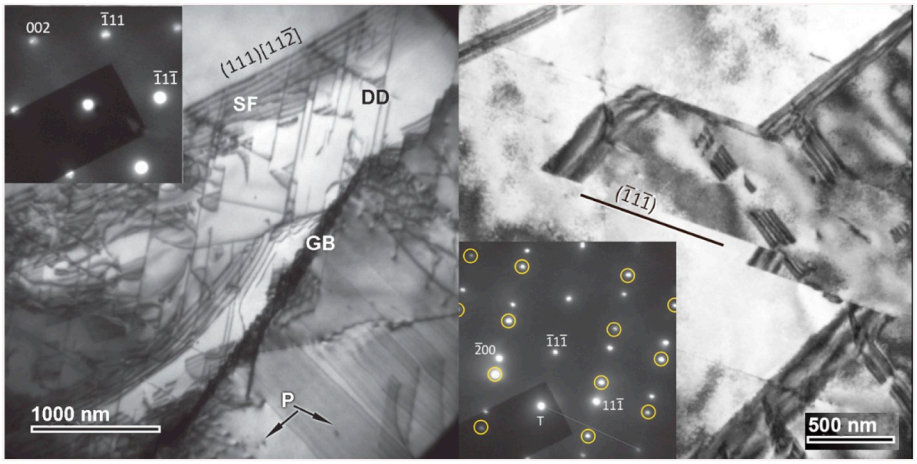

Fig. 16. Same alloy as in Fig. 14 but annealed at 1000 °C, sample **J**. No dislocations are seen in the matrix. The low magnification TEM images show the interaction between defects: a) effect of a grain boundary on stacking faults and dissociated dislocations. A few small precipitates are indicated by black arrows. b) Effect of a twin inhibiting the development of the SFs. The inset corresponds to a SAEDP where the circled reflections are due to the twin. Zone axis [001]γ.

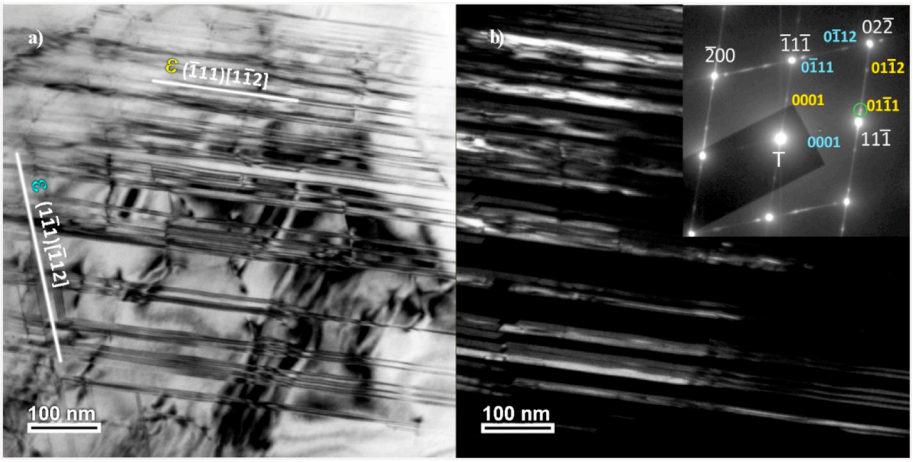

Fig. 17. Microstructure of the 17Mn alloy rolled at 1000 °C and annealed at 700 °C after 4% tensile deformation at room temperature, sample **Ct**. a) A bright field image showing ε-martensite in two variants. b) Dark field image taken from the circled spot. The zone axes of the diffraction pattern are [011]γ //[11$\bar{2}$0]ε.

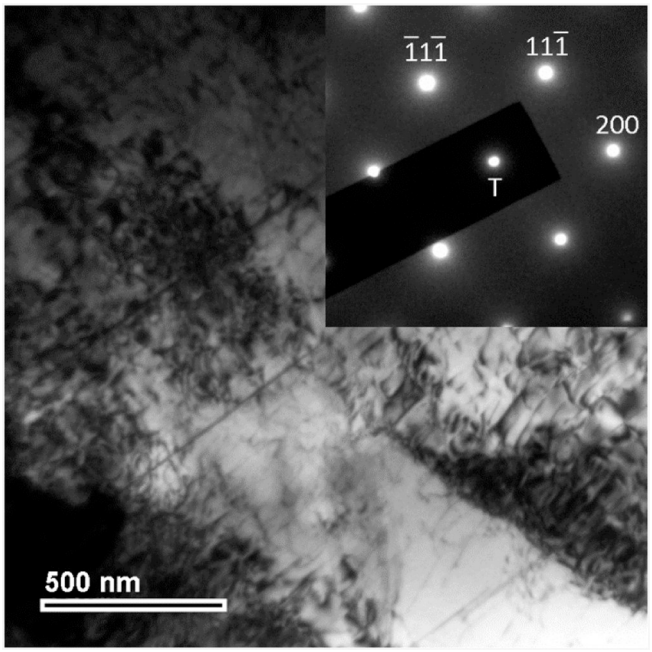

Fig. 18. Microstructure of the 22Mn alloy rolled at 1000 °C and annealed at 700 °C after 4% tensile deformation at room temperature, sample **Ht**. The bright field image shows a few thin ε-martensite plates, a high density of dislocations and SFs. The zone axis of the diffraction pattern is [011]γ.

source of SFs.

X-ray diffraction patterns clearly showed the presence of the $Fe_5Ni_3Si_2$ phase, in the 17Mn alloy and to a lesser extent in the 22Mn alloy (see Fig. 5). The size, distribution and density of the precipitates were described from the OM images shown in Fig. 6. Although the precipitates can be present in the as-homogenised condition, annealing at 800 °C activates massive precipitation. This is consistent with previous investigations that showed that precipitation occurs during recovery annealing between 600 and 900 °C [27].

Second phase particles can be either beneficial or have a negligible effect on the SM behaviour. The precipitates located at grain boundaries do not affect the SM properties [35]. Instead, if they are dispersed into the austenite matrix they can subdivided grains into smaller areas and can act as obstacles to martensitic growth. Consequently, during deformation they and their resultant strain fields can prevent the impingement of martensite bands belonging to different small areas [36]. This obviates the relaxation of the back stresses as a result of plastic accommodation, which would necessarily occur at martensitic intersections. Thus, the reversibility of stress-induced martensite formation can be remarkably improved and the SME enhanced [37].

A low SFE, which is a necessary condition for the SME, also affects austenite strengthening, due to the subdivision of grains by dislocation boundaries [38]. We observed the formation of different dislocation microstructures in both materials, when they were annealed at temperatures lower than that for recrystallization. These microstructures would be another factor inhibiting plastic deformation, particularly during tension to induce the γ → ε martensitic transformation in the

17Mn samples, which have the lower SFE.

Finally, the austenitic matrix of samples **E** and **J** is so weak that its yield stress is lower than the stress to induce the martensitic transformation, $\sigma_{\gamma\rightarrow\varepsilon}$. The DSRs for these samples were the lowest among all the conditions tested for each alloy.

Rolling at 1000 °C followed by annealing at 700 °C is the thermo-mechanical treatment that developed the best microstructural characteristics related to shape memory behaviour in this alloys. The analysis of samples **Ct** and **Ht**, performed after deformation to induce the martensitic transformation, highlights the issue. TEM micrographs from sample **Ct** are shown in Fig. 17. Stress-induced ε-martensite grew in two variants, but preferentially formed along the tensile direction in specifically oriented γ grains. The plates' thickness was < 12 nm. The matrix is composed of dislocations, SFs and precipitates, similar to that observed in sample **C**, i.e. before deformation. On the other hand, after tension, few thin ε-martensite plates developed in the 22Mn alloy rolled at 1000 °C and annealed at 700 °C. The density of dislocations observed is higher than that observed before tension, which proves that the stress applied to induce the martensitic transformation could first (or simultaneously) activate dislocation glide and multiplication. The low 48% DSR is thus a consequence of permanent, nonrecoverable plastic deformation.

5. Conclusions

We studied the shape memory behaviour of Fe-17Mn-6Si-10Cr-5Ni and Fe-22Mn-3Si-10Cr-5Ni alloys. Particularly, we concentrated on the effect of the microstructures obtained after thermo-mechanical treatments that provide a range of grain sizes combining with good mechanical and shape memory properties. Using these compositions, the presence of the detrimental ferrite phase was avoided in all the processing conditions. Shape memory tests showed that the behaviour of the 17Mn alloy is much better than that of the 22Mn composition. The best degree of shape recovery was achieved after rolling at 1000 °C followed by annealing at 700 °C.

In summary, our detailed microstructural characterizations highlighted the following features:

1) Nanotwins (about 10 nm) harden the austenite parent phase and thus, improve the DSR. They appear in the 17Mn alloy after rolling at 650 °C and annealing at 700 °C (sample **A**).
2) Thick twins (about 1000–1100 nm) negatively affect the shape recovery, since they impede partial dislocation movement (samples **E**, **G**, **I** and **J**)
3) The $Fe_5Ni_3Si_2$ precipitates improve the reversibility of the stress-induced martensite and thus enhance the SME. The 17Mn alloy has a greater content of this second phase than the 22Mn alloy.
4) The samples annealed at 1000 °C show the least amount of shape recovery among all the conditions studied. The absence of dislocations weakens the austenitic matrices so that samples can deform plastically, rather than through the martensitic transformation.
5) The ε-martensite plate thickness is nanometre sized in samples **Ct** and **Ht**. However, the quantity of plates is lower in the latter material and the microstructural pattern has changed after tension to induce the martensitic transformation. For the 22Mn alloy rolled at 1000 °C and annealed at 700 °C, the dislocation density increased with tensile deformation. This proves that in this case the stress applied to induce the martensitic transformation first (or simultaneously) activated dislocation glide and multiplication. The low 48% DSR is thus a consequence of permanent, nonrecoverable plastic deformation.

Data availability

The raw data required to reproduce these findings are available to download from https://cloud.rosario-conicet.gov.ar/s/MArmSf5KU22hM9C.

No processed data are required to reproduce these findings.

Acknowledgements

The authors acknowledge financial support from ANPCyT (PICT 2016-1460), CIN-CONICET (PDTS-251) and SCyT-UNR (PID ING579). We also thank Dr. Natalia De Vincentis for the XR-measurements and refinements, and Dr. M. Stout for proofreading this manuscript.

References

[1] K. Otsuka, C.M. Wayman, Shape Memory Materials, Cambridge University Press, Cambridge, 1998.
[2] T. Omori, R. Kainuma, Materials science: alloys with long memories, Nature 502 (2013) 42–44, https://doi.org/10.1126/science.1202232.
[3] O. Matsumura, T. Sumi, N. Tamura, K. Sakao, T. Furukawa, H. Otsuka, Pseudoelasticity in an Fe–28Mn–6Si–5Cr shape memory alloy, Mater. Sci. Eng. A 279 (2000) 201–206, https://doi.org/10.1016/S0921-5093(99)00644-9.
[4] A. Sato, E. Chishima, K. Soma, T. Mori, Shape memory effect in γ→ε transformation in Fe-30Mn-1Si alloy single crystals, Acta Metall. 30 (1982) 1177–1183, https://doi.org/10.1016/0001-6160(82)90011-6.
[5] M. Sade, A. Baruj, H.E. Troiani, FCC/HCP martensitic transformation temperatures and thermal cycling evolution in Fe-Mn-Cr alloys, New Dev Metall Appl High Strength Steels Buenos Aires 2008, 1, 2 Wiley-VCH Verlag GmbH & Co, 2008, p. 87339.
[6] H. Otsuka, H. Yamada, T. Maruyama, H. Tanahashl, S. Matsuda, M. Murakami, Effects of alloying additions on Fe-Mn-Si shape memory alloys, ISIJ Int. 30 (1990) 674–679, https://doi.org/10.2355/isijinternational.30.674.
[7] H. Otsuka, H. Yamada, H. Tanahashi, T. Maruyama, Shape memory effect in Fe-Mn-Si-Cr-Ni polycrystalline alloys, Mater. Sci. Forum 56–58 (1990) 655–660, https://doi.org/10.4028/www.scientific.net/MSF.56-58.655.
[8] M.J. Lai, Y.J. Li, L. Lillpopp, D. Ponge, S. Will, D. Raabe, On the origin of the improvement of shape memory effect by precipitating VC in Fe-Mn-Si-based shape memory alloys, Acta Mater. 155 (2018) 222–235, https://doi.org/10.1016/j.actamat.2018.06.008.
[9] S. Kajiwara, Characteristic features of shape memory effect and related transformation behavior in Fe-based alloys, Mater. Sci. Eng. A 273–275 (1999) 67–88, https://doi.org/10.1016/S0921-5093(99)00290-7.
[10] D.Z. Liu, S. Kajiwara, T. Kikuchi, N. Shinya, Atomic force microscopy study on microstructural changes by 'training' in Fe-Mn-Si-based shape memory alloys, Philos. Mag. 83 (2003) 2875–2897, https://doi.org/10.1080/14786043031000149090.
[11] K. Ogawa, S. Kajiwara, HREM study of stress-induced transformation structures in an Fe-Mn-Si-Cr-Ni shape memory alloy, Mater. Trans. JIM 34 (1993) 1169–1176.
[12] S. Kajiwara, D. Liu, T. Kikuchi, N. Shinya, Remarkable improvement of shape memory effect in Fe-Mn-Si based shape memory alloys by producing NbC precipitates, Scr. Mater. 44 (2001) 2809–2814, https://doi.org/10.1016/S1359-6462(01)00978-2.
[13] S. Kajiwara, D. Liu, Z.T. Kikuchi, N. Shinya, Development of Fe-Mn-Si based shape memory alloys with no necessity of "training", J. Phys. IV 11 (2001) 199–204.
[14] N. Stanford, D.P. Dunne, Effect of NbC and TiC precipitation on shape memory in an iron-based alloy, J. Mater. Sci. 41 (2006) 4883–4891, https://doi.org/10.1007/s10853-006-0050-7.
[15] N. Stanford, D.P. Dunne, Effect of second-phase particles on shape memory in Fe-Mn-Si-based alloys, Mater. Sci. Eng. A 454–455 (2007) 407–415, https://doi.org/10.1016/j.msea.2006.11.084.
[16] A. Baruj, H.E. Troiani, The effect of pre-rolling Fe–Mn–Si-based shape memory alloys: mechanical properties and transmission electron microscopy examination, Mater. Sci. Eng. A 481–482 (2008) 574–577, https://doi.org/10.1016/j.msea.2007.02.140.
[17] A. Druker, A. Baruj, J. Malarría, Effect of rolling conditions on the structure and shape memory properties of Fe–Mn–Si alloys, Mater. Charact. 61 (2010) 603–612, https://doi.org/10.1016/j.matchar.2010.03.005.
[18] O. Söderberg, X.W. Liu, P.G. Yakovenko, K. Ullakko, V.K. Lindroos, Corrosion behaviour of Fe-Mn-Si based shape memory steels trained by cold rolling, Mater. Sci. Eng. A 273–275 (1999) 543–548, https://doi.org/10.1016/S0921-5093(99)00396-2.
[19] V. Paleu, G. Gurău, R.I. Comăneci, V. Sampath, C. Gurău, L.G. Bujoreanu, A new application of Fe-28 Mn-6 Si-5 Cr (mass. %) shape memory alloy, for self-adjustable axial preloading of ball bearings, Smart Mater. Struct. 27 (7) (2018), https://doi.org/10.1088/1361-665X/aac4c5.
[20] A.M. Balagurov, I.A. Bobrikov, J. Pons, J. Cifre, L.Y. Sun, I.S. Golovin, Structure of the Fe-Mn-Si alloys submitted to γ↔ε thermocycling, Mater. Charact. 141 (2018) 223–228, https://doi.org/10.1016/j.matchar.2018.04.052.
[21] H. Ju, C. Lin, Z. Liu, J. Zhang, Study of in-situ formation of Fe-Mn-Si shape memory alloy welding seam by laser welding with filler powder, Opt. Laser Technol. 104 (2018) 65–72, https://doi.org/10.1016/j.optlastec.2018.01.062.
[22] Y.S. Kim, E. Choi, W.J. Kim, Characterization of the microstructures and the shape memory properties of the Fe-Mn-Si-Cr-Ni-C shape memory alloy after severe plastic deformation by differential speed rolling and subsequent annealing, Mater. Charact. 136 (2018) 12–19, https://doi.org/10.1016/j.matchar.2017.11.055.

[23] H. Peng, G. Wang, S. Wang, J. Chen, I. MacLaren, Y. Wen, Key criterion for achieving giant recovery strains in polycrystalline Fe-Mn-Si based shape memory alloys, Mater. Sci. Eng. A 712 (2018) 37–49, https://doi.org/10.1016/j.msea.2017.11.071.

[24] A. Druker, P. Vermaut, J. Malarría, The shape recovery conditions for Fe–Mn–Si alloys: an interplay between martensitic transformation and plasticity, Mater. Charact. 139 (2018) 319–327, https://doi.org/10.1016/j.matchar.2018.03.018.

[25] A. Druker, P. La Roca, P. Vermaut, P. Ochin, J. Malarría, Microstructure and shape memory properties of Fe–15Mn–5Si–9Cr–5Ni melt-spun ribbons, Mater. Sci. Eng. A 556 (2012) 936–945, https://doi.org/10.1016/j.msea.2012.07.097.

[26] A.V. Druker, A. Perotti, I. Esquivel, J. Malarría, A manufacturing process for shaft and pipe couplings of Fe–Mn–Si–Ni–Cr shape memory alloys, Mater. Des. 56 (2014) 878–888, https://doi.org/10.1016/j.matdes.2013.11.032.

[27] V. Fuster, A.V. Druker, A. Baruj, J. Malarría, R. Bolmaro, Characterization of phases in an Fe–Mn–Si–Cr–Ni shape memory alloy processed by different thermo-mechanical methods, Mater. Charact. 109 (2015) 128–137, https://doi.org/10.1016/j.matchar.2015.09.026.

[28] G. Wang, H. Peng, C. Zhang, S. Wang, Y. Wen, Relationship among grain size, annealing twins and shape memory effect in Fe–Mn–Si based shape memory alloys, Smart Mater. Struct. 25 (2016) 075013.

[29] Y.H. Wen, H.B. Peng, D. Raabe, I. Gutierrez-Urrutia, J. Chen, Y.Y. Du, Large recovery strain in Fe-Mn-Si-based shape memory steels obtained by engineering annealing twin boundaries, Nat. Commun. 5 (2014) 4964, , https://doi.org/10.1038/ncomms5964.

[30] J.C. Li, M. Zhao, Q. Jiang, Alloy design of FeMnSiCrNi shape-memory alloys related to stacking-fault energy, Metall. Mater. Trans. A 31A (2000) 581, https://doi.org/10.1007/s11661-000-0001-x.

[31] J.T. Benzing, W.A. Poling, D.T. Pierce, J. Bentley, K.O. Findley, D. Raabe, J.E. Wittig, Effects of strain rate on mechanical properties and deformation behavior of an austenitic Fe-25Mn-3Al-3Si TWIP-TRIP steel, Mater. Sci. Eng. A 711 (2018) 78–92, https://doi.org/10.1016/j.msea.2017.11.017.

[32] M. Meyer, L. Murr, A model for the formation of annealing twins in F.C.C. metals and alloys, Acta Metall. 26 (6) (1978) 951–962, https://doi.org/10.1016/0001-6160(78)90046-9.

[33] H. Inagaki, Shape memory effect of Fe-14%Mn-6%Si-9%Cr-6%Ni alloy polycrystals, Z. Metallkd. 83 (1992) 90–96.

[34] P. Kürnsteiner, C. Commenda, E. Arenholz, L. Samek, D. Stifter, H. Groiss, Investigation of nanoscale twinning in an advanced high manganese twinning-induced plasticity steel, Materialia 1 (2018) 70–77, https://doi.org/10.1016/j.mtla.2018.04.001.

[35] H. Peng, L. Yong, S. Wang, Y. Wen, Role of annealing in improving shape memory effect of as-cast Fe-Mn-Si-Cr-Ni shape memory alloys, Metall. Mater. Trans. A (2019), https://doi.org/10.1007/s11661-019-05233-w.

[36] Y.H. Wen, L.R. Xiong, N. Li, W. Zhang, Remarkable improvement of shape memory effect in an Fe–Mn–Si–Cr–Ni–C alloy through controlling precipitation direction of Cr23C6, Mater. Sci. Eng. A 474 (2008) 60–63, https://doi.org/10.1016/j.msea.2007.05.043.

[37] A. Arabi-Hashemi, W.J. Lee, C. Leinenbach, Recovery stress formation in FeMnSi based shape memory alloys: impact of precipitates, texture and grain size, Mater. Des. 139 (2018) 258–268, https://doi.org/10.1016/j.matdes.2017.11.006.

[38] D. Hughes, A. Godfrey, Dislocation structures formed during hot and cold working, Conference: Hot Deformation of Aluminium Alloys II, Rosemont, IL (US), SAND98-8490C, 1998.